Mapping of vibrational modes revealing a strong and tunable coupling in two juxtaposed 3R-WSe2 nanodrums

Anis Chiout, Cléophanie Brochard-Richard, Fabrice Oehler, Abdelkarim Ouerghi, Julien Chaste

Mapping of vibrational modes revealing a strong and tunable coupling in two juxtaposed 3R-WSe_2 nanodrums

Anis Chiout[1], Cléophanie Brochard-Richard[1], Fabrice Oehler [1], Abdelkarim Ouerghi [1], Julien Chaste [1*]

[1]Université Paris-Saclay, CNRS, Centre de Nanosciences et de Nanotechnologies, 91120, Palaiseau, France.

* Corresponding author: julien.chaste@universite-paris-saclay.fr

Abstract:

Two-dimensional (2D) material resonators have emerged as promising platforms for advanced nanomechanical applications due to their exceptional mechanical properties, tunability, and non-linearities. We explore the strong mechanical mode coupling between two adjacent 3R-WSe_2 nanodrums at room temperature. Combining a piezoelectric material, as non-centrosymmetric 3R-WSe_2, and vibration manipulation is the building block for phononic experiments with 2D materials. By strategically placing gate grids beneath each resonator and by mapping the spatial distribution of these modes, we demonstrate the ability to transit between localized modes in individual membranes to delocalized, strongly coupled modes that span the entire suspended region. The coherent coupling is strongly tunable with simple gate voltage and remarkable resonance splitting was achieved, corresponding to up to 5% of the vibration frequency. These results showcase the potential of 2D material resonators for efficient information exchange, paving the way for novel applications in quantum technologies and nanoscale sensing.

Keywords: 2D materials , strong coupling, nanomechanic, phononic, tunability, TMDs

---

In recent years, nanomechanical systems that incorporate two-dimensional (2D) resonators have demonstrated remarkable characteristics, including high-quality factors[1–4] and exceptional modulation of mechanical vibrations.[5,6] They have high Young's modulus and exceptional resistance to mechanical stress. Due to their atomic thickness, 2D mechanical resonators are both robust and highly extensible.[7] Additionally, they have been implemented to generate mechanical frequency combs and to couple tunable modes. [8–11] Furthermore, 2D mechanical

resonators have low mass and low spring constants. It makes them suitable for detecting low mass or force, [1,12,13] as well as for high-performance bolometers[14] and sensitive spectrometers.[15] 2D resonators possess another captivating aspect, which relates to their tunable and non-linear physics. Non-linearities often dominate their equations of motion, such as the duffing term[16] or the damping term.[17,18] These can be employed to manipulate the resonators modes,[19] and they are even expected to take an even greater importance in the quantum vibration regime. [20]
With the recent progress in device fabrication and mechanical mode engineering, it is now feasible to couple the various vibrational modes of one[21,22] or more[11,23] 2D resonators[24] For example, it was possible to fabricate a tunable phononic resonator with a graphene membrane.[25] The coherent coupling[10,26] between modes causes an extremely effective exchange of energy[27] between them. This highlights the potential of 2D mechanical resonators in phonon propagation, information exchange, and quantum computing using classical systems, even at room temperature.[28] The control over the mechanical coupling between two resonators is a critical building block for future experiments in the phononic domain with an array of resonators. It is remarkable that phononic waveguides have been previously reported by combining piezoelectric materials and series of juxtaposed membranes.[29] A 2D material with such properties are the Rhombohedral bilayer TMDs,[30,31] due to a non-centrosymmetric and sliding ferroelectricity at ambient.[32,33]

Two-dimensional (2D) material resonators have shown significant strong coupling between modes of different resonators at very low temperatures [9,11,21,24,26,34,35] as well between modes of the same resonator at room temperature.[8] In this study, we investigate a system consisting of two adjacent 3R-WSe_2 nanodrums whose vibrational modes physically overlap. Our aim is to explore the properties of this system and to examine the mode coupling between the two drums. In order to extend to phononic, it is important to consider a coupling with pure mechanical origin since electrostatic coupling is difficult to achieve for assembly of resonators.[10,36] Multiple resonators have been mechanically coupled via small beams[37,38], via substrate, [23,26] or via juxtaposed mechanical modes. [29,39] Our system differs from previous investigations[11,23] by the physical nature of the coupling, which is here purely mechanical and important compared to mechanical frequency. Up to now, such very strong coupling between mechanical resonators has only been reported at low temperature using graphene[23] or through the electrostatic coupling of SiC nanowires[36]. A discussion through the spatial and frequency mapping of mechanical mode, allows us to assess the similarities and difference between the coupled modes between two separate nanodrums and the fundamental modes of a combined larger membrane.

To start our fabrication process, we first produce bilayer single-crystal WSe_2 flakes stacked vertically in a 3R configuration, by chemical vapour deposition (CVD).[31] This particular 3R symmetry is non-centrosymmetric and can lead to interesting piezoelectric and phononic experiments using 2D materials. Our CVD-grown 3R-WSe_2 bilayers are then transferred from the growth substrate (SiO_2/Si) to a host substrate which holds electrical contacts fabricated by standard cleanroom processing, in the form of two connected holes in an 8-shaped configuration. The 2D material is pick up using an HQ graphene transfer station and a PMMA resin. The resin is then annealed at 350°C in a vacuum. Most importantly, each hole is individually gated at its base to selectively address the corresponding vibration by electrostatic means and contacted to source and drain via the voltage V_{DS}.

As depicted in Figure 1-a and 1-b, the local and independent electrostatic gates of the circular membranes are labelled V_{G1} and V_{G2} for the membrane 1 and the membrane 2, respectively. By varying the individual gate voltages (V_{Gi}), we apply a local capacitive force on the membrane i, $F_{il} = -\frac{1}{2}\,{\partial C_{p,il}}/{\partial z_{il}}\,V_{Gi}^2$ with $C_{p,il}$ the capacitance between the membrane i and its gate contact l. The parameter z_{il} is the vertical spatial separation between the related membrane and gate contact. This capacitive force modifies the stiffness of membrane i as $k_i(V_{Gi})$ [40]. The pairing between each membrane and its gate thus allows one to individually tune the resonance frequency of each nanodrum, modelled as a conventional mechanical oscillator $\omega_i = \sqrt{k_i/m_i}$ with m_i its effective mass and ω_i the vibration frequency.

Lock-in techniques are used to measure the mechanical movements. Here, the membranes motion is actuated by adding a small sinusoidal voltage (a few tens of millivolts) to the static gate voltage (V_{Gi}). The vibrations of the nanodrums are measured optically, using laser interferometry (red laser, λ=632 nm).[5,19,41,42] This optical arrangement is very sensitive to the membrane movement due to the formation of a Fabry-Pérot cavity between the top 2D material and the bottom gold gates. The laser power is adapted to ensure a reduced photothermal effect in our samples (see supplementary information S4).

In addition to the local gates V_{G1} and V_{G2} below the membrane, a pair of two large electrical contacts encloses the two resonators in a standard horizontal transistor arrangement. One contact is used to apply a global V_{DS} voltage.

At V_{G1}=0 V, V_{G2}=-5 V and V_{DS} = 0 V, the membranes labelled 1 and 2 vibrate at frequencies $\omega_1 = 28.31 \times 2\pi$ MHz and $\omega_2 = 29.77 \times 2\pi$ MHz, respectively, with quality factors of Q_1=163 and Q_2=201 (Figure1-d). The slight intrinsic frequency difference between membranes 1 and 2 is possibly due to an imperfect geometry of the two SiO_2 holes. Different pre-deformation or strain distribution acquired during the fabrication process could also explain this difference. Yet, we consider this small difference as minimal in the context of 2D material resonators.

In the following, we investigate the vibration modes ω_1 and ω_2 as a function of the electrostatic strain applied to the membranes. Figure 1-e shows the dependence $\omega_1(V_{G1})$ and $\omega_2(V_{G2})$ in the specific case where $V_G = V_{G1} = V_{G2}$. Both membranes exhibit the same behavior with respect to V_G. For $|V_G|$ <15 V, we first observe a decrease in the resonance frequency due to capacitive softening.[43] Then, for $|V_G|$ >15 V both membranes stiffen ($k \propto V_G^2$) [41] and the resonant frequency increases[41]. We also observe a third mechanical mode, in Figure 1-e, ω_3 around 33 MHz.

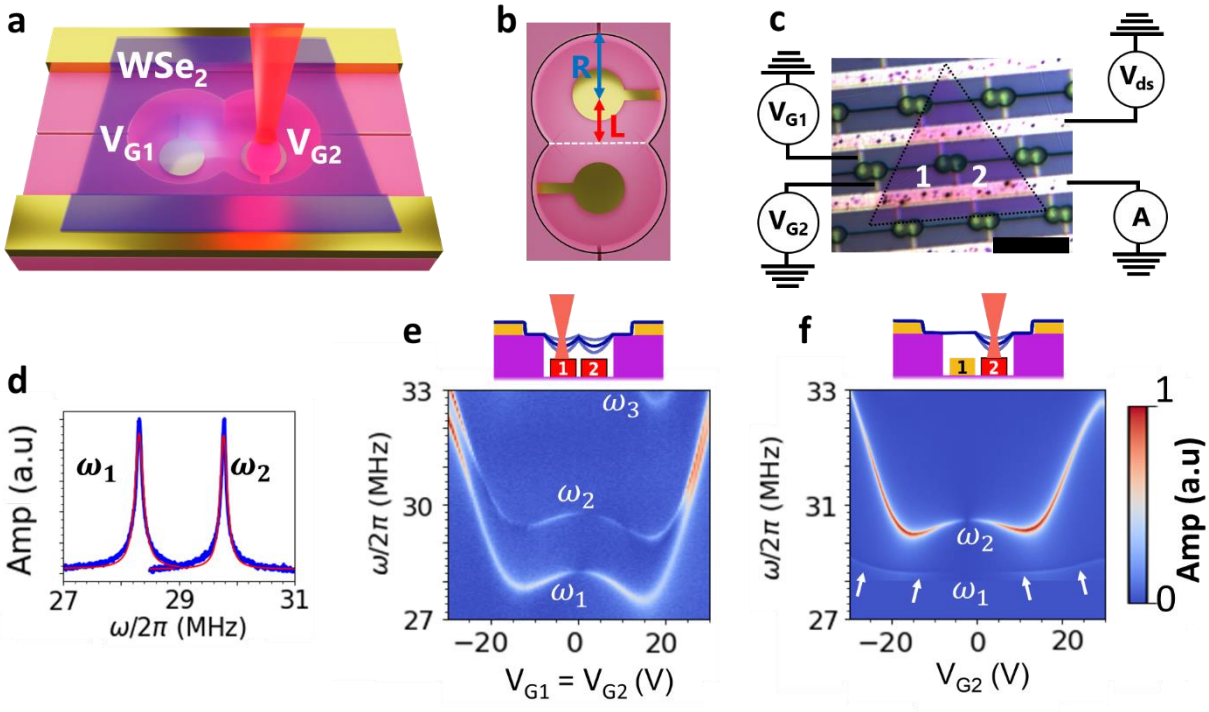

Figure 1 - The dual gated 8-shaped WSe_2 nanodrums. (a) Opto-electromechanical platform based on two local gates to excite each nanodrum individually and a red laser to measure the vibrations. (b) Schematic top view of the device, showing the nanodrum radius R and separation

L. (c) Optical image of the sample. The WSe_2 flake appears as purple triangle on the image. The nanodrums are labelled 1 and 2. V_{ds} is for the source drain voltage applied to measure the transversal current along the sample. Scale bar = 10 µm (d) The resonant frequency of the two nanodrums taken at $V_{G1}=V_{G2}=V_G$ = -5 V. (e) Variation of the mechanical vibration of the drums ω_1, ω_2, and ω_3 as a function of V_{G1}/V_{G2}. Both gates are activated at the same time and have the same excitation and voltage. (f). Variation of ω_2 with respect to V_{G2} with V_{G1} = 0 V with excitation and measurement on nanodrum 2. The gate used for the excitation of the membrane is marked with a red colour on the corresponding schematic when activated.

Figure 1- f shows the independent variation of ω_2 as a function of V_{G2} when V_{G1} is grounded. We see that $\omega_2$varies in the same way as in Figure 1- e while we have weak dependencies $\omega_1(V_{G2})$ and $\omega_2(V_{G1})$. A zoom of ω_1 is shown in supplementary information part S9. For these two uncoupled modes, we consider that the capacitive force of gate 1 over membrane 2 is weak (Figure 1-f) and vice versa (Figure 2-a) which translates mathematically as $(F_{12}, F_{21} \ll F_{11}, F_{22})$.

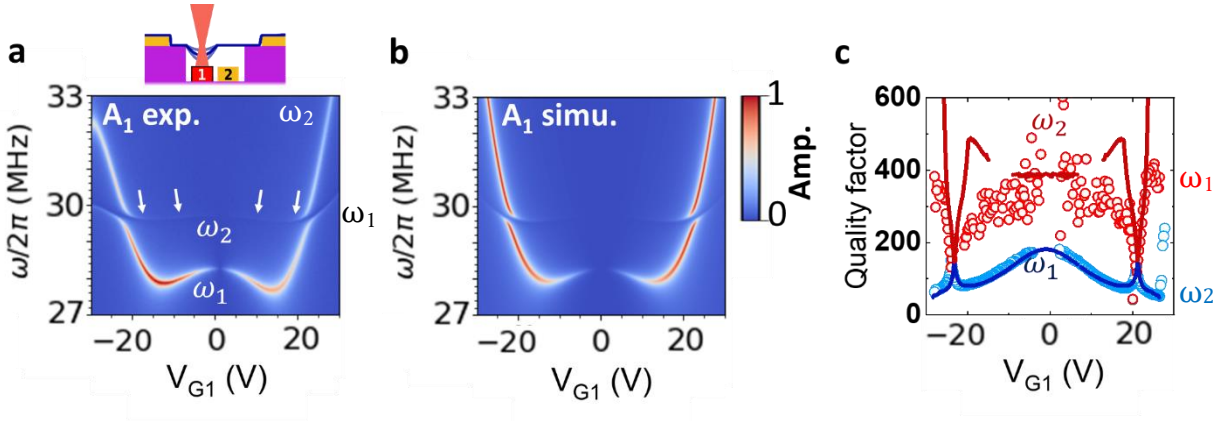

Figure 2 - Two modes-coupling. (a) Variation of ω_1 with respect to V_{G1} with V_{G2} = 0 V with excitation and measurement on nanodrum 1. An anti-crossing is observed at $V_{G1} = +21\ V$. (b) Corresponding numerical computation of the measurement of the movement amplitude A_1 (1). (c) Quality factor of the modes ω_1 and ω_2 with respect to V_{G1} extracted from measurement (circles) and from simulation (lines). Outside of the coupling area, the quality factors are distinct and become equal at the coupling region, which is an indicator of strong coupling.

In the first set of measurements, Figure 1-d and Figure 1-e show that there is no crossover of the frequencies ω_1 and ω_2. To highlight the coupling between the two nanodrums, we study the variation of ω_1 as a function of V_{G1} (Figure 2-a) with V_{G2}=0 V. We observe the same variation of ω_1 frequency as in Figure 1-e, while ω_2 hardly varies similarly to the Figure 1-f. An important difference, compared to Figure 1-e, is the anti-crossing of the frequency curves, $\omega_1 = \omega_2$ near V_{G1} = ±22 V which indicates a strong coupling between the two mechanical modes. We define the experimental resonance peak splitting 2g, related to the intermodal coupling strength j, as being the minimum frequency difference between the two modes in Figure 2-a. The measured value is g = 255 kHz.

To describe both the uncoupled region and the mode coupling, we consider the following coupled motion equations[27,11]:

$$\begin{cases} \ddot{x}_1 + \gamma_1 \dot{x}_1 + \omega_{01}^2 x_1 = j x_2 + f_d \cos(\omega_d t) \\ \ddot{x}_2 + \gamma_2 \dot{x}_2 + \omega_{02}^2 x_2 = j x_1 \end{cases} \qquad (1)$$

With x_i the oscillatory amplitude of each membrane vibration, ω_{0i} are the natural frequencies of the two modes. f_d the driving force, ω_d the driving frequency and $\gamma_i = \omega_i / Q_i$ the damping rates of each membrane. To find the solutions of the equation (1), as previously described in references [27,11], the system has to be diagonalized. In Figure 2b, we recover the two frequencies $\omega_{1,2}$ of the coupled resonators. We extract and simulate the amplitude of both modes A_i defined by $x_i(t) = A_i(\cos \omega_d t + \phi_i)$.

For our system, we expect a pure mechanical coupling, as in a tug-of-war contest in which both resonators exercise forces on the shared part of the membrane. Compared to reference[11], the studied mechanical modes spatially overlap and the electrical resistance is low.

In the numerical simulation in Figure 2-b, we obtain g = 255 kHz and j = 2.10^{15} Hz^2 to reproduce the experimental variations. This gives a cooperativity $c = \frac{(2g)^2}{\gamma_1 \gamma_2} = 6.2$. The coupling is considered strong if the cooperativity $c > 1$, so we conclude on the strong coupling between these two modes.

As the model describes the dissipations of the resonators, in Figure 2-c, we compare the experimental quality factors Q_i of each resonator (open symbol) extracted from the Lorentzian fits on our measurements and those derived from numerical model (solid line). We observe a reasonable quantitative match between theory and experiment. Most importantly, our model

captures a critical feature of the anti-crossing ($V_{G1} = \pm 22\ V$), where the quality factors of each membrane collapse to a single value. Outside the anti-crossing region, we measure a low Q_1 and a high Q_2. Such increase of dissipation and widening of the peaks in membrane 1 is expected since both electrical and laser excitations are applied on membrane 1. At the anti-crossing, Q_1 slightly increases from 90 to 175 while Q_2 sharply decreases from 400 to 175. Under such strong coupling conditions, mechanical energy is exchanged between the two modes and this indicates that the two mechanical modes share the same energy dissipation channels at the anti-crossing.[44]

The modes share the same dissipation channels in the anti-crossing zone. A plausible assumption is that the modes are also spatially delocalised and superimposed. To address this, we present a systematic mapping of the distinct modes in our devices between coupled and decoupled regimes. We displace the probe laser over the drum surface holding all static voltages constant. The amplitude and phase of the vertical membrane motion are then measured by interferometry.

Let discuss about the results. Far from the anti-crossing, (V_{G1}=15 V, V_{G2}=0 V), the normalized amplitudes $|A|$ of the two modes are shown in Figures 3-a and 3-b. We observe two circular modes at frequencies ω_1 and ω_2 spatially localised on membrane 1 and 2, respectively. In first approximation, we could consider that these are both fundamental modes of the circular membrane, characterized by a node index n=0. The modes show a limited spatial overlap. However, it can be seen in the ω_2 mode that the drum 1 vibrates slightly when the drum 2 is excited, this is not an artefact but the signature of a residual coupling between the two membranes and a consequence of a greater stiffness of membrane 2, which pulls on membrane 1. This is confirmed by numerical simulations.

In Figure 3-c and 3-d, we map the normalized amplitude ($|A|\cos(\varphi)$) taking in account the phase φ of the vibration of the ω_1 and ω_2 branches in the couple drum regime, close to the anti-crossing (V_{G1}=-21V, V_{G2}=0V) [42]. Each mode spatially extends to the other drum in a significant way. We can consider the modes as delocalised along the whole suspended membrane. The inner structure of each branch is now apparent: at $|V_{G1}|$ = 22 V, ω_1 is the in-phase summation of the natural modes ω_{01} and ω_{02} while ω_2 combines those fundamentals but in phase opposition. The two membranes vibrate collectively and the branches resemble the two first harmonic

modes, n=0 and n=1, of a combined elliptical membrane of width 2R and length (2R+2L). We also measure and simulate the mode ω_3 in supplementary information Part S11.

In Figure 3-e, we test the hypothesis of the spatial delocalization of collective mode ω_1 by selectively exciting the mode ω_1 using gate 1 or gate 2. It is not affected by the spatial origin of the actuating gate voltage, which is characteristic of a delocalized mode.

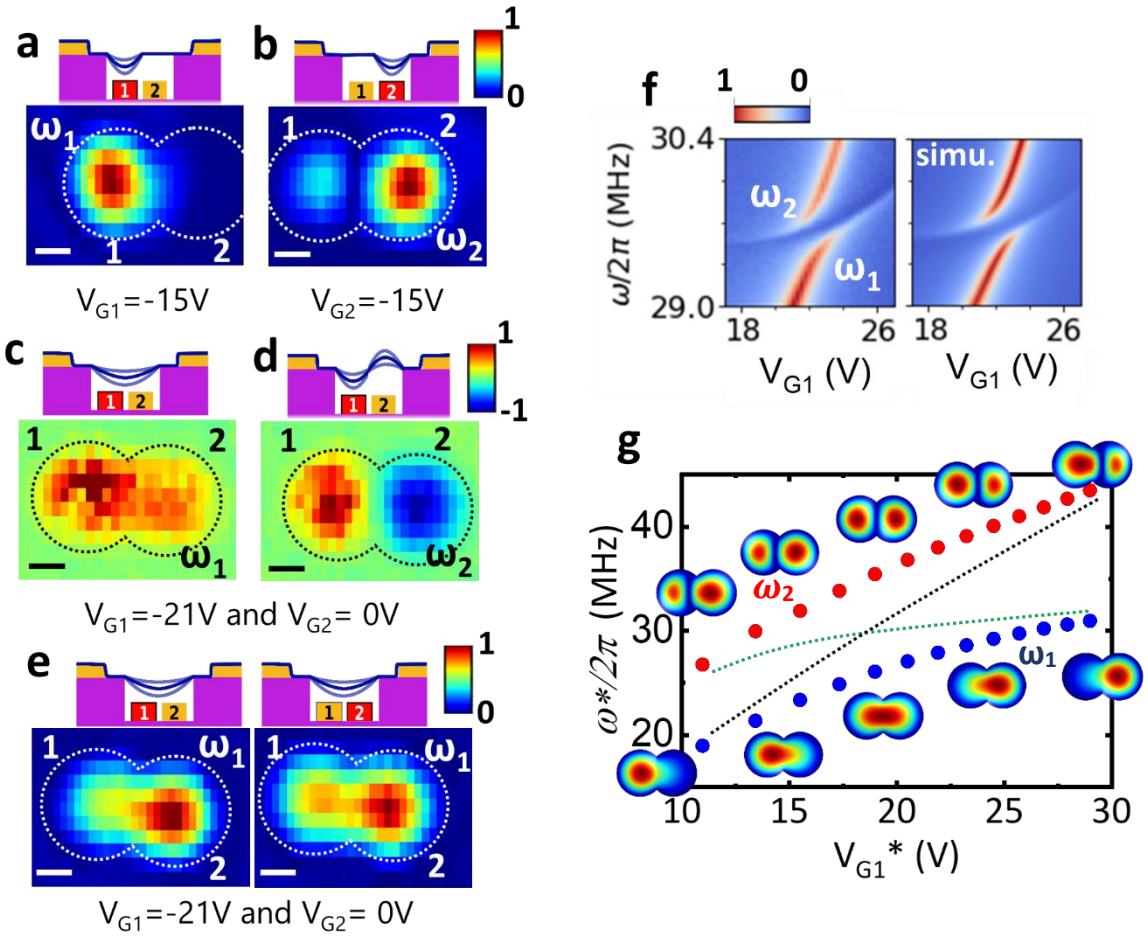

Figure 3 – Cartography of the vibrational modes. a) Shape of the amplitude of the circular mode ω_1 at $V_{G1} = -15\ V, V_{G2} = 0\ V$. b) Shape of the amplitude of the mode ω_2 at $V_{G1} = 0\ V, V_{G2} = -15\ V$. c) and d) Maps of the ω_1 and ω_2 modes taking into account the phase of vibration of both sides. e) Amplitude of the vibrational mode ω_1 with excitations at gate 1 and 2 (indicated in red in the scheme). All scale bars: 1 μm. f) Zoom in the coupling region of the measurement and simulation of the modes ω_1 and ω_2. g) Simulation of the shape of the modes ω_1 and ω_2 using COMSOL with different values of stiffness for membrane 1. The green and black dotted lines guide the eye to the situation of two uncoupled and natural modes.

The Figure 3g shows a numerical simulation, using COMSOL finite element modelling of the shape of the mechanical modes ω_1 and ω_2 of our 8-shaped resonator without bending stiffness.

We obtain two localized modes behaving as strongly coupled modes with an anti-crossing when the frequencies matched in qualitative agreement with the experimental dispersion diagram of Figure 3-f. Our simulation is only mechanic and does not consider capacitive effects as in ref [11]. The boundary between membrane 1 and membrane 2 is defined by a straight line that divides the device equally in two homogenous strains. It defines two local spring constants: k_2^* which is kept constant and k_1^* which varies linearly. k_1^* correspond to a gate bias using $V_{G1}^* \propto \sqrt{k_1^*}$, which corresponds to the parabolic stiffening regime ($|V_{G1}|>15$ V). We have also schematically represented the resonance frequencies of the two uncoupled natural modes ω_{02} and ω_{01}. When $\omega_1 < \omega_2$, away from the–anti-crossing, the mode ω_1 is confined within the borders of membrane 1 while ω_2 is mostly present on the membrane 2 with a small contribution on drum 1. When we approach the anti-crossing, the modes become more delocalized on the surface of both membranes until the spatial extension is maximized at the anti-crossing. There, we observe a good agreement between the simulated mechanical coupling and measurements in Figure 3 c, 3 g and 3 e.

Even if we qualitatively reproduce the spatial features of the modes at the anti-crossing, the frequency difference $\Delta f=2g$ at the ω_1/ω_2 anti-crossing quantitatively differs between our experiment $\Delta f_{exp}=510$ kHz and the COMSOL simulation $\Delta f_{sim}=9.4$ MHz by more than a decade. This suggests that the experiment is not well reproduced by simulations but it suggests also that the mechanical coupling must be huge and, certainly, is at the origin of the strong coupling in our experiment.

Since we experimentally observe different resonance frequencies ($\omega_1 \neq \omega_2$) at $V_{G1} = V_{G2} = 0\ V$), we know that the spatial strain distribution over the whole membrane is likely to be more complex. [45]

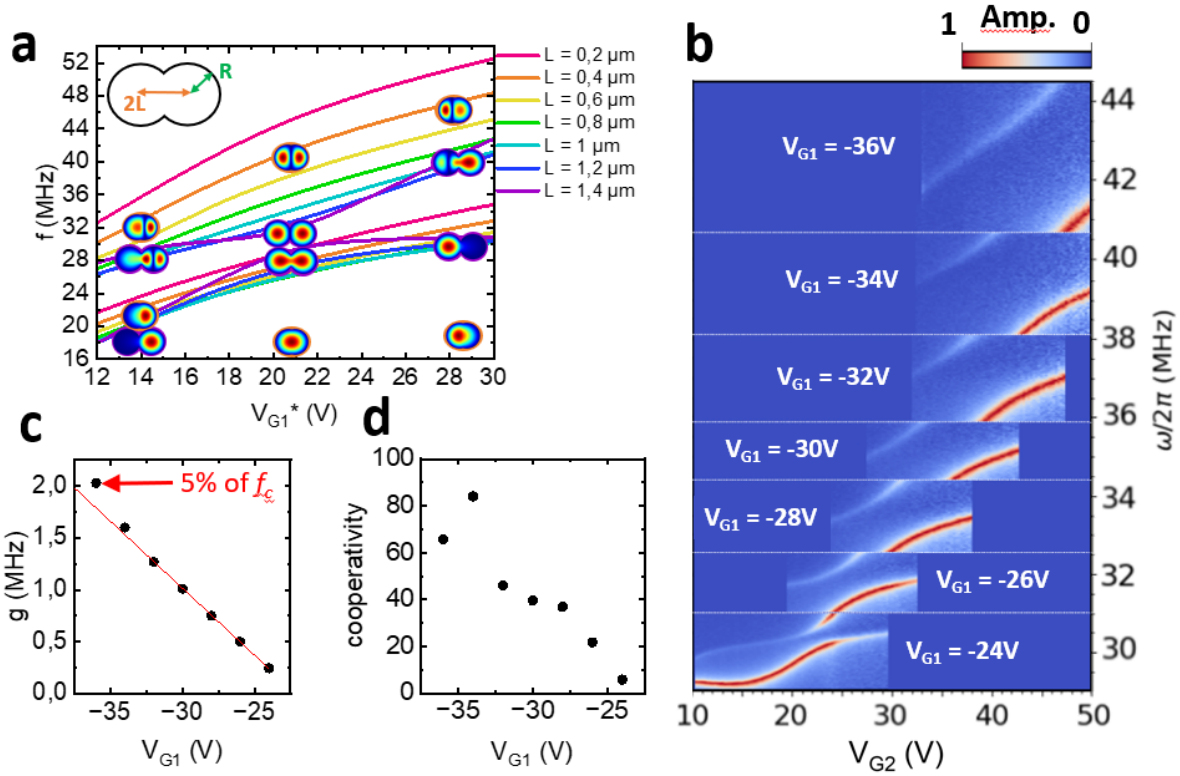

Figure 4 – Tunable strong coupling frequency. a) Simulations of resonant frequencies in function of V_{G1} ∗ for different Length L (the sample has a length L=0.85 µm). The inset displays the corresponding coupling strength in percent of the resonance frequency. The red arrow indicates our device b) The two mechanical resonances in the anti-crossing region in function of ω and V_{G2} for different V_{G1} between -24 V and -36 V. c) The peak splitting difference 2g increases with the gate voltage applied to membrane 1. The red line is a guideline for eye. d) Cooperativity as a function of V_{G1}.

We propose to explore the effect of the geometry in our system and to get a better understanding and perspective of the observed mechanical coupling. In Figure 4-a, we vary the distance L between the two resonators in our COMSOL simulations, while maintaining constant the radius R of each drum. The native strain is considered homogenous. Using our experimental fabrication parameter,L=0.85 µm, we obtain a theoretical value of g=15% of ω which we can compare to our experimental value of g <1% of ω. At the limit L=0 (ie. a single resonator), the two superimposed modes become the n=0 and n=1 uncoupled harmonic of a circular membrane and $\omega_2/\omega_1 = 1.6$ as expected.[35] In this specific case, the two gates will be too close ($F_{12}, F_{21} \approx F_{11}, F_{22}$) to measure anything and the system is not anymore similar to a tug-of-war game.

To investigate the discrepancy between the theoretical and experimental values of the frequency difference g, the Figure 4-b represents the modulation of the frequency and the coupling strength g in our system by tuning V_{G1}. Excitation and optical measurements are performed on

membrane 2. The gate bias $V_{G1}$is sweep from -24 V to -36 V. The resonance peak splitting and the coupling strength are modulated by an order of magnitude (g = 250 kHz to g = 2.05 MHz) as shown in Figure 4-d. In the Figure 4-d, the cooperativity c is increased by a factor 11 between V_{G1} = -24 V and V_{G1} = -36 V. The obtained c=66 represents a very strong coupling at room temperature. We are then able to reach a factor g up to g = 5% of ω knowing that 10% is the limit to ultra-strong coupling.[46,47]

We notice, but do not explain, that g depends almost linearly on V_{G1}. It does not converge asymptotically to the simulated value of 15% limit but tend to sub linearly diverge above 5%. The frequency difference between the two modes, is large and fixed in the simulation, whereas it is lower and tunable in our experiment. Our simplified model has certain limitations and does not define the real limit of our system.

This result paves the way for the measurement of ultra-strong coupling by coupling two 2D mechanical resonators. Especially since it was recently demonstrated on circular membranes made from 2D materials that it was possible to apply a very high gate voltage. [48] In this work, we studied mechanical resonators of 2D materials physically coupled and the tunable coupling between these vibrations. We studied the differences between the uncoupled and coupled modes of vibration by mapping the latter, showing the confinement of the uncoupled modes and the delocalisation of the coupled modes. Next, we were able to achieve very strong coupling regimes with frequency difference g=5% of the vibration frequency. In references [25,29] and in phononic devices in general, 1D or 2D arrays of resonators are considered, connected together by small beams or coupled with a localized mode overlapping as in our device. In reference [29], the coupling between two adjacent resonators is weak. Our work represents the basic element for future applications in phononic with possible 2D piezoelectric, and with a tunable and strong coupling.

We pointed out the similarities and differences between a two circular-drum device and a dual gated 8-shaped resonator due to our dual gate configuration which tune independently the spring constant of half the 8 shaped resonators. At L=0 µm, the two modes are superimposed and they are different harmonics of an oscillator.[49,50] Under our experimental conditions, L=0.85 µm, and beyond, we clearly observe an anti-crossing region. An intermediate regime must exist between the two cases. However, in 2D materials, it is possible to hybridize or couple these modes together due to the tunability of vibrations in the membranes of 2D materials.[8,51]

Supplementary material: It includes additional Atomic force microscopy, optical measurements, photocurrent measurements and multiple additional material for the mechanical measurements as non-linearities and coupling measurements.

Acknowledgments: The work was supported by French grants ANR ANETHUM (ANR-19-CE24-0021), ANR Deus-nano (ANR-19-CE42-0005), ANR 2DHeco (ANR-20-CE05-0045), and (ANR-22-PEXD-0006) FastNano project, as well as the French technological network RENATECH.

Data avaibility: The data that support the findings of this study are available from the corresponding author upon reasonable request.

Bibliography

(1) Chen, C.; Rosenblatt, S.; Bolotin, K. I.; Kalb, W.; Kim, P.; Kymissis, I.; Stormer, H. L.; Heinz, T. F.; Hone, J. Performance of Monolayer Graphene Nanomechanical Resonators with Electrical Readout. *Nat. Nanotechnol.* **2009**, *4* (12), 861–867. https://doi.org/10.1038/nnano.2009.267.

(2) Xu, B.; Zhang, P.; Zhu, J.; Liu, Z.; Eichler, A.; Zheng, X.-Q.; Lee, J.; Dash, A.; More, S.; Wu, S.; Wang, Y.; Jia, H.; Naik, A.; Bachtold, A.; Yang, R.; Feng, P. X.-L.; Wang, Z. Nanomechanical Resonators: Toward Atomic Scale. *ACS Nano* **2022**, *16* (10), 15545–15585. https://doi.org/10.1021/acsnano.2c01673.

(3) Ferrari, P. F.; Kim, S.; van der Zande, A. M. Nanoelectromechanical Systems from Two-Dimensional Materials. *Appl. Phys. Rev.* **2023**, *10* (3), 031302. https://doi.org/10.1063/5.0106731.

(4) Bachtold, A.; Moser, J.; Dykman, M. I. Mesoscopic Physics of Nanomechanical Systems. *Rev. Mod. Phys.* **2022**, *94* (4), 045005. https://doi.org/10.1103/RevModPhys.94.045005.

(5) Chiout, A.; Brochard-Richard, C.; Marty, L.; Bendiab, N.; Zhao, M.-Q.; Johnson, A. T. C.; Oehler, F.; Ouerghi, A.; Chaste, J. Extreme Mechanical Tunability in Suspended MoS2 Resonator Controlled by Joule Heating. *Npj 2D Mater. Appl.* **2023**, *7* (1), 1–8. https://doi.org/10.1038/s41699-023-00383-3.

(6) Ying, Y.; Zhang, Z.-Z.; Moser, J.; Su, Z.-J.; Song, X.-X.; Guo, G.-P. Sliding Nanomechanical Resonators. *Nat. Commun.* **2022**, *13* (1), 6392. https://doi.org/10.1038/s41467-022-34144-5.

(7) Bertolazzi, S.; Brivio, J.; Kis, A. Stretching and Breaking of Ultrathin MoS2. *ACS Nano* **2011**, *5* (12), 9703–9709. https://doi.org/10.1021/nn203879f.

(8) Prasad, P.; Arora, N.; Naik, A. K. Gate Tunable Cooperativity between Vibrational Modes. *Nano Lett.* **2019**. https://doi.org/10.1021/acs.nanolett.9b01219.

(9) Luo, G.; Zhang, Z.-Z.; Deng, G.-W.; Li, H.-O.; Cao, G.; Xiao, M.; Guo, G.-C.; Tian, L.; Guo, G.-P. Strong Indirect Coupling between Graphene-Based Mechanical Resonators via a Phonon Cavity. *Nat. Commun.* **2018**, *9* (1), 383. https://doi.org/10.1038/s41467-018-02854-4.

(10) Zhang, Z.-Z.; Song, X.-X.; Luo, G.; Su, Z.-J.; Wang, K.-L.; Cao, G.; Li, H.-O.; Xiao, M.; Guo, G.-C.; Tian, L.; Deng, G.-W.; Guo, G.-P. Coherent Phonon Dynamics in Spatially Separated Graphene Mechanical Resonators. *Proc. Natl. Acad. Sci.* **2020**, *117* (11), 5582–5587. https://doi.org/10.1073/pnas.1916978117.

(11) Šiškins, M.; Sokolovskaya, E.; Lee, M.; Mañas-Valero, S.; Davidovikj, D.; van der Zant, H. S. J.; Steeneken, P. G. Tunable Strong Coupling of Mechanical Resonance between Spatially Separated $FePS_3$ Nanodrums. *Nano Lett.* **2022**, *22* (1), 36–42. https://doi.org/10.1021/acs.nanolett.1c03010.

(12) Jiang, C.; Li, Q.; Huang, J.; Bi, S.; Ji, R.; Guo, Q. Single-Layer MoS2 Mechanical Resonant Piezo-Sensors with High Mass Sensitivity. *ACS Appl. Mater. Interfaces* **2020**, *12* (37), 41991–41998. https://doi.org/10.1021/acsami.0c11913.

(13) Kumar, M.; Bhaskaran, H. Ultrasensitive Room-Temperature Piezoresistive Transduction in Graphene-Based Nanoelectromechanical Systems. *Nano Lett.* **2015**, *15* (4), 2562–2567. https://doi.org/10.1021/acs.nanolett.5b00129.
(14) Blaikie, A.; Miller, D.; Alemán, B. J. A Fast and Sensitive Room-Temperature Graphene Nanomechanical Bolometer. *Nat Commun* **2019**, *10*, 4726.
(15) Kirchhof, J. N.; Yu, Y.; Yagodkin, D.; Stetzuhn, N.; Araújo, D. B. de; Kanellopulos, K.; Manas-Valero, S.; Coronado, E.; Zant, H. van der; Reich, S.; Schmid, S.; Bolotin, K. I. Nanomechanical Absorption Spectroscopy of 2D Materials with Femtowatt Sensitivity. *2D Mater.* **2023**, *10* (3), 035012. https://doi.org/10.1088/2053-1583/acd0bf.
(16) Davidovikj, D.; Alijani, F.; Cartamil-Bueno, S. J.; van der Zant, H. S. J.; Amabili, M.; Steeneken, P. G. Nonlinear Dynamic Characterization of Two-Dimensional Materials. *Nat. Commun.* **2017**, *8* (1), 1253. https://doi.org/10.1038/s41467-017-01351-4.
(17) Eichler, A.; Moser, J.; Chaste, J.; Zdrojek, M.; Wilson-Rae, I.; Bachtold, A. Nonlinear Damping in Mechanical Resonators Made from Carbon Nanotubes and Graphene. *Nat. Nanotechnol.* **2011**, *6* (6), 339–342. https://doi.org/10.1038/nnano.2011.71.
(18) Keşkekler, A.; Shoshani, O.; Lee, M.; van der Zant, H. S. J.; Steeneken, P. G.; Alijani, F. Tuning Nonlinear Damping in Graphene Nanoresonators by Parametric–Direct Internal Resonance. *Nat. Commun.* **2021**, *12* (1), 1099. https://doi.org/10.1038/s41467-021-21334-w.
(19) Chiout, A.; Correia, F.; Zhao, M.-Q.; Johnson, A. T. C.; Pierucci, D.; Oehler, F.; Ouerghi, A.; Chaste, J. Multi-Order Phononic Frequency Comb Generation within a MoS2 Electromechanical Resonator. *Appl. Phys. Lett.* **2021**, *119* (17), 173102. https://doi.org/10.1063/5.0059015.
(20) Samanta, C.; De Bonis, S. L.; Møller, C. B.; Tormo-Queralt, R.; Yang, W.; Urgell, C.; Stamenic, B.; Thibeault, B.; Jin, Y.; Czaplewski, D. A.; Pistolesi, F.; Bachtold, A. Nonlinear Nanomechanical Resonators Approaching the Quantum Ground State. *Nat. Phys.* **2023**, 1–5. https://doi.org/10.1038/s41567-023-02065-9.
(21) Liu, C.-H.; Kim, I. S.; Lauhon, L. J. Optical Control of Mechanical Mode-Coupling within a MoS2 Resonator in the Strong-Coupling Regime. *Nano Lett.* **2015**, *15* (10), 6727–6731. https://doi.org/10.1021/acs.nanolett.5b02586.
(22) Li, S.-X.; Zhu, D.; Wang, X.-H.; Wang, J.-T.; Deng, G.-W.; Li, H.-O.; Cao, G.; Xiao, M.; Guo, G.-C.; Jiang, K.-L.; Dai, X.-C.; Guo, G.-P. Parametric Strong Mode-Coupling in Carbon Nanotube Mechanical Resonators. *Nanoscale* **2016**, *8* (31), 14809–14813. https://doi.org/10.1039/C6NR02853E.
(23) Zhang, Z.-Z.; Song, X.-X.; Luo, G.; Su, Z.-J.; Wang, K.-L.; Cao, G.; Li, H.-O.; Xiao, M.; Guo, G.-C.; Tian, L.; Deng, G.-W.; Guo, G.-P. Coherent Phonon Dynamics in Spatially Separated Graphene Mechanical Resonators. *Proc. Natl. Acad. Sci.* **2020**, *117* (11), 5582–5587. https://doi.org/10.1073/pnas.1916978117.
(24) Mathew, J. P.; Patel, R. N.; Borah, A.; Vijay, R.; Deshmukh, M. M. Dynamical Strong Coupling and Parametric Amplification of Mechanical Modes of Graphene Drums. *Nat. Nanotechnol.* **2016**, *11* (9), 747–751. https://doi.org/10.1038/nnano.2016.94.
(25) Kirchhof, J. N.; Weinel, K.; Heeg, S.; Deinhart, V.; Kovalchuk, S.; Höflich, K.; Bolotin, K. I. Tunable Graphene Phononic Crystal. *Nano Lett.* **2021**, *21* (5), 2174–2182. https://doi.org/10.1021/acs.nanolett.0c04986.
(26) Okamoto, H.; Gourgout, A.; Chang, C.-Y.; Onomitsu, K.; Mahboob, I.; Chang, E. Y.; Yamaguchi, H. Coherent Phonon Manipulation in Coupled Mechanical Resonators. *Nat. Phys.* **2013**, *9* (8), 480–484. https://doi.org/10.1038/nphys2665.
(27) Zanette, D. H. Energy Exchange between Coupled Mechanical Oscillators: Linear Regimes. *J. Phys. Commun.* **2018**, *2* (9), 095015. https://doi.org/10.1088/2399-6528/aadfc6.
(28) Tsai, C.-Y.; Kuo, W.-T.; Lin, C.-B.; Chen, T.-L. Design and Fabrication of MEMS Logic Gates. *J. Micromechanics Microengineering* **2008**, *18* (4), 045001. https://doi.org/10.1088/0960-1317/18/4/045001.

(29) Hatanaka, D.; Mahboob, I.; Onomitsu, K.; Yamaguchi, H. Phonon Waveguides for Electromechanical Circuits. *Nat. Nanotechnol.* **2014**, *9* (7), 520–524. https://doi.org/10.1038/nnano.2014.107.
(30) Mahmoudi, A.; Bouaziz, M.; Chapuis, N.; Kremer, G.; Chaste, J.; Romanin, D.; Pala, M.; Bertran, F.; Fèvre, P. L.; Gerber, I. C.; Patriarche, G.; Oehler, F.; Wallart, X.; Ouerghi, A. Quasi van Der Waals Epitaxy of Rhombohedral-Stacked Bilayer WSe2 on GaP(111) Heterostructure. *ACS Nano* **2023**, *17* (21), 21307–21316. https://doi.org/10.1021/acsnano.3c05818.
(31) Mahmoudi, A.; Bouaziz, M.; Chiout, A.; Di Berardino, G.; Ullberg, N.; Kremer, G.; Dudin, P.; Avila, J.; Silly, M.; Derycke, V.; Romanin, D.; Pala, M.; Gerber, I. C.; Chaste, J.; Oehler, F.; Ouerghi, A. Electronic Properties of Rhombohedrally Stacked Bilayer WSe2 Obtained by Chemical Vapor Deposition. *Phys. Rev. B* **2023**, *108* (4), 045417. https://doi.org/10.1103/PhysRevB.108.045417.
(32) Chang, C.; Zhang, X.; Li, W.; Guo, Q.; Feng, Z.; Huang, C.; Ren, Y.; Cai, Y.; Zhou, X.; Wang, J.; Tang, Z.; Ding, F.; Wei, W.; Liu, K.; Xu, X. Remote Epitaxy of Single-Crystal Rhombohedral WS2 Bilayers. *Nat. Commun.* **2024**, *15* (1), 4130. https://doi.org/10.1038/s41467-024-48522-8.
(33) Jiang, H.; Li, L.; Wu, Y.; Duan, R.; Yi, K.; Wu, L.; Zhu, C.; Luo, L.; Xu, M.; Zheng, L.; Gan, X.; Zhao, W.; Wang, X.; Liu, Z. Vapor Deposition of Bilayer 3R MoS2 with Room-Temperature Ferroelectricity. *Adv. Mater.*, 2400670. https://doi.org/10.1002/adma.202400670.
(34) Singh, R.; Sarkar, A.; Guria, C.; Nicholl, R. J. T.; Chakraborty, S.; Bolotin, K. I.; Ghosh, S. Giant Tunable Mechanical Nonlinearity in Graphene–Silicon Nitride Hybrid Resonator. *Nano Lett.* **2020**, *20* (6), 4659–4666. https://doi.org/10.1021/acs.nanolett.0c01586.
(35) Alba, R. D.; Massel, F.; Storch, I. R.; Abhilash, T. S.; Hui, A.; McEuen, P. L.; Craighead, H. G.; Parpia, J. M. Tunable Phonon-Cavity Coupling in Graphene Membranes. *Nat. Nanotechnol.* **2016**, *11* (9), 741–746. https://doi.org/10.1038/nnano.2016.86.
(36) Perisanu, S.; Barois, T.; Poncharal, P.; Gaillard, T.; Ayari, A.; Purcell, S. T.; Vincent, P. The Mechanical Resonances of Electrostatically Coupled Nanocantilevers. *Appl. Phys. Lett.* **2011**, *98* (6), 063110. https://doi.org/10.1063/1.3553779.
(37) Madiot, G. Optomechanical Generation of Coherent GHz Vibrations in a Phononic Waveguide. *Phys. Rev. Lett.* **2023**, *130* (10). https://doi.org/10.1103/PhysRevLett.130.106903.
(38) Safavi-Naeini, A. H.; Hill, J. T.; Meenehan, S.; Chan, J.; Gröblacher, S.; Painter, O. Two-Dimensional Phononic-Photonic Band Gap Optomechanical Crystal Cavity. *Phys. Rev. Lett.* **2014**, *112* (15), 153603. https://doi.org/10.1103/PhysRevLett.112.153603.
(39) Wang, Y.; Lee, J.; Zheng, X.-Q.; Xie, Y.; Feng, P. X.-L. Hexagonal Boron Nitride Phononic Crystal Waveguides. *ACS Photonics* **2019**, *6* (12), 3225–3232. https://doi.org/10.1021/acsphotonics.9b01094.
(40) Chen, C.; Deshpande, V. V.; Koshino, M.; Lee, S.; Gondarenko, A.; MacDonald, A. H.; Kim, P.; Hone, J. Modulation of Mechanical Resonance by Chemical Potential Oscillation in Graphene. *Nat. Phys.* **2016**, *12* (3), 240–244. https://doi.org/10.1038/nphys3576.
(41) Chaste, J.; Hnid, I.; Khalil, L.; Si, C.; Durnez, A.; Lafosse, X.; Zhao, M.-Q.; Johnson, A. T. C.; Zhang, S.; Bang, J.; Ouerghi, A. Phase Transition in a Memristive Suspended MoS2 Monolayer Probed by Opto- and Electro-Mechanics. *ACS Nano* **2020**, *14* (10), 13611–13618. https://doi.org/10.1021/acsnano.0c05721.
(42) Davidovikj, D.; Slim, J. J.; Cartamil-Bueno, S. J.; van der Zant, H. S. J.; Steeneken, P. G.; Venstra, W. J. Visualizing the Motion of Graphene Nanodrums. *Nano Lett.* **2016**, *16* (4), 2768–2773. https://doi.org/10.1021/acs.nanolett.6b00477.
(43) Wu, C. C.; Zhong, Z. Capacitive Spring Softening in Single-Walled Carbon Nanotube Nanoelectromechanical Resonators. *Nano Lett.* **2011**, *11* (4), 1448–1451. https://doi.org/10.1021/nl1039549.
(44) Verbiest, G. J.; Goldsche, M.; Sonntag, J.; Khodkov, T.; Driesch, N. von den; Buca, D.; Stampfer, C. Tunable Coupling of Two Mechanical Resonators by a Graphene Membrane. *2D Mater.* **2021**, *8* (3), 035039. https://doi.org/10.1088/2053-1583/ac005e.
(45) Sarafraz, A.; Liu, H.; Cvetanović, K.; Spasenović, M.; Vollebregt, S.; Manzaneque Garcia, T.; Steeneken, P. G.; Alijani, F.; Verbiest, G. J. Quantifying Stress Distribution in Ultra-Large

Graphene Drums through Mode Shape Imaging. *Npj 2D Mater. Appl.* **2024**, *8* (1), 1–8. https://doi.org/10.1038/s41699-024-00485-6.
(46) Frisk Kockum, A.; Miranowicz, A.; De Liberato, S.; Savasta, S.; Nori, F. Ultrastrong Coupling between Light and Matter. *Nat. Rev. Phys.* **2019**, *1* (1), 19–40. https://doi.org/10.1038/s42254-018-0006-2.
(47) Bayer, A.; Pozimski, M.; Schambeck, S.; Schuh, D.; Huber, R.; Bougeard, D.; Lange, C. Terahertz Light–Matter Interaction beyond Unity Coupling Strength. *Nano Lett.* **2017**, *17* (10), 6340–6344. https://doi.org/10.1021/acs.nanolett.7b03103.
(48) Hernández López, P.; Heeg, S.; Schattauer, C.; Kovalchuk, S.; Kumar, A.; Bock, D. J.; Kirchhof, J. N.; Höfer, B.; Greben, K.; Yagodkin, D.; Linhart, L.; Libisch, F.; Bolotin, K. I. Strain Control of Hybridization between Dark and Localized Excitons in a 2D Semiconductor. *Nat. Commun.* **2022**, *13* (1), 7691. https://doi.org/10.1038/s41467-022-35352-9.
(49) Wang, Z.; Lee, J.; He, K.; Shan, J.; Feng, P. X.-L. Embracing Structural Nonidealities and Asymmetries in Two-Dimensional Nanomechanical Resonators. *Sci. Rep.* **2014**, *4*. https://doi.org/10.1038/srep03919.
(50) Wang, Z.; Lee, J.; Feng, P. X.-L. Spatial Mapping of Multimode Brownian Motions in High-Frequency Silicon Carbide Microdisk Resonators. *Nat. Commun.* **2014**, *5* (1), 5158. https://doi.org/10.1038/ncomms6158.
(51) Güttinger, J.; Noury, A.; Weber, P.; Eriksson, A. M.; Lagoin, C.; Moser, J.; Eichler, C.;Wallraff, A.; Isacsson, A.; Bachtold, A. (2017). Energy-dependent path of dissipation in nanomechanical resonators. Nature nanotechnology, 12(7), 631-636.